MOLECULAR GAS DYNAMICS OF THE LENSED WET-MERGER RXSJ1131-1123 AT Z=0.654

T. K. DAISY LEUNG AND DOMINIK A. RIECHERS

Department of Astronomy, Space Sciences Building, Cornell University, Ithaca, NY 14853, USA; tleung@astro.cornell.edu

To be submitted to the ApJ

ABSTRACT

Subject headings: ISM: molecular – infrared: galaxies – galaxies: mergers – galaxies: starburst – galaxies: evolution

1. INTRODUCTION

We use a concordance ΛCDM cosmology throughout this paper, with parameters from the WMAP9 results: H_0 = 70 km s^{-1} Mpc^{-1}, Ω_M = 0.27, and Ω_Λ = 0.7 (Hinshaw et al. 2013).

2. OBSERVATIONS

2.1. *PdBI CO(J = 2 → 1)*

Observations of the CO($J = 2 \rightarrow 1$) rotational line ($\nu_{\rm rest}$ = 230.5379938 GHz) toward the gravitationally lensed galaxy RXJ1131-1231 at $z_{\rm QSO} = 0.658$ were carried out using IRAM Plateau de Bure Interferometer (PdBI; Program ID: S14BX001; PI: D. Riechers). Two observing runs were carried out on 2014 December 06 and 2015 February 05 under good weather conditions in the C and D array configurations, respectively. The 2 mm receivers were used to cover the redshifted CO($J = 2 \rightarrow 1$) line and the underlying continuum emission, employing a correlator setup providing an effective bandwidth of 3.6 GHz and a spectral resolution of 10.0 MHz (~ 21.5 km s^{-1}). This resulted in 3.75 hours of cumulative six antenna-equivalent on-source time after discarding unusable visibility data. The nearby quasars 1127−145 and 1124−186 were observed every 22 minutes for pointing, secondary amplitude, and phase calibration and 1055+018 was observed as the bandpass calibrator for both tracks. MWC349 and 3C279 were observed as the primary flux calibrator for C and D array observations, respectively, yielding $\lesssim$15% calibration accuracy.

The GILDAS package was used to reduce and analyze the visibility data which are then imaged and deconvolved using the CLEAN algorithm with "natural" weighting. This yields a synthesized clean beam size of 4.′′44 × 1.′′95 (PA = 13°). The final rms noise is σ = 1.451 mJy km s^{-1} beam^{-1} over 10 MHz (21.5 km s^{-1}). The continuum image at $\nu_{\rm cont} \sim 139$ GHz is created by averaging over all the line-free channels. This yields an rms noise of 0.082 mJy beam^{-1}.

2.2. *CARMA CO(J = 3 → 2)*

Observations of the CO($J = 3 \rightarrow 2$) rotational line ($\nu_{\rm rest}$ = 345.7959899 GHz) were carried out under the D array configurations of the Combined Array for Research in Millimeter-wave Astronomy (CARMA; Program ID: cf0098; PI: D. Riechers) on 2014 February 02 under terrible 1.5 mm weather conditions and on 2014 February 17

under good 1.5 mm weather conditions. The correlator setup provides a bandwidth of 3.75 GHz in each sideband and a spectral resolution of 12.5 MHz ($\sim$17.9 km s^{-1}). The line was placed in the lower sideband with the local oscillator tuned to $\nu_{\rm LO} \sim 216$ GHz. The radio quasars J1127−189 (first track) and 3C273 (second track) were observed every 15 minutes for pointing, amplitude, and phase calibration. Mars was observed as the primary absolute flux calibrator and 3C279 was observed as the bandpass calibrator for both tracks. This results in a total on-source time of 2.94 hours after flagging poor visibility data.

Given that the phase calibrator used for the first track was faint and was observed under poor weather conditions and that the phase calibrator used for the second track was far from our target source, the phase calibration is subpar, with an rms scatter $\sim$60°. We thus conservatively estimate a calibration accuracy of $\sim$45% based on the flux scale uncertainties, the gain variations over time, and the phase scatter on the calibrated data. We therefore treat its line intensity with caution and ensure that any physical interpretation of this system (and thus implications and conclusions of this paper) do not rely on this quantity.

The MIRIAD package was used to calibrate the visibility data which are then imaged and deconvolved using the CLEAN algorithm with "natural" weighting. This yields a synthesized clean beam size of 3.′′2 × 1.′′9 (PA = 8°) for the lower sideband image cube. The final rms noise is σ = 13.3 mJy km s^{-1} beam^{-1} over a channel width of 25 MHz. An rms noise of σ = 0.831 mJy beam^{-1} is reached by averaging over the line-free channels.

2.3. *VLA*

Our analysis also use the archival data of the radio continuum obtained with the *Karl G. Jansky* Very Large Array (VLA; Program ID: AW741; PI: Wucknitz). Since the observations have not been described in any previous publications, we here describe their details as well as our calibration steps.

Observations were carried out on 2008 December 29 under excellent weather conditions in the A array configurations for a total of $\sim$7 hours on-source time. The C−band receivers were used with a continuum mode setup, providing a bandwidth of 50 MHz in each sideband. The nearby radio quasar 1130−149 was observed every 10 minutes for pointing, amplitude, and phase calibration, 1331−305 was observed as the primary flux calibrator, and 0319+415 was observed as the bandpass calibrator, yielding $\sim$10% cal-

ibration accuracy. We use AIPS to calibrate the visibility data which are then imaged and deconvolved using the CLEAN algorithm using robust = 0. This yields a synthesized clean beam size of $0.''49 \times 0.''35$ (PA = $0.''18$) and a final rms noise of $\sigma = 13 \,\mu$Jy beam^{-1}.

3. HST ASTROMETRY

We obtain *HST* images from the Hubble Legacy Archive with a goal to understand the origins of the emission detected in our mm observations. We adopt the VLA 5 GHz map of $\sim 0.''5$ resolution as the reference coordinate frame to align the optical (V-band) image. We shift the latter to the east by $0.''5963$ in R.A. and $+0.''8372$ in Dec., which is consistent with the typical astrometric precision $(1-2'')$ of images from the Hubble Legacy Archive[1]. Such astrometric correction is critical to avoid artificial spatial offsets between different emitting regions and to carry out our lens modeling, in which the absolute position of the foreground lensing galaxy is guided by its coordinates in the optical image, where its emission is clearly detected. The VLA image is calibrated using a well-monitored phase calibrator, with absolute positional accuracy of ~ 2 mas. For this reason, the absolute alignment between the VLA image and other interferometric images reported in this paper are expected to have astrometric precision better than $0.''1$, modulo uncertainties related to the SNR, phase errors, and beam size.

4. RESULTS

4.1. *CO(J = 2 → 1) Emission*

We dynamically resolved the CO($J = 2 \to 1$) line emission toward the background galaxies at $\gtrsim 27\sigma$ significance, confirming the redshift at $z_{\rm CO} = 0.65370 \pm 0.0005$. A highly asymmetric double-horned line profile is detected as shown in Figure 1. Fitting a double Gaussian results in peak flux densities of 75.3 ± 2.6 and 24.0 ± 2.0 mJy, and a FWHM of 179 ± 9 km s^{-1} and 255 ± 28 km s^{-1}, respectively. The peaks are separated by $\Delta v_{\rm sep} = 220$ km s^{-1}. The integrated line flux is 24.1 ± 2.3 Jy km s^{-1}.
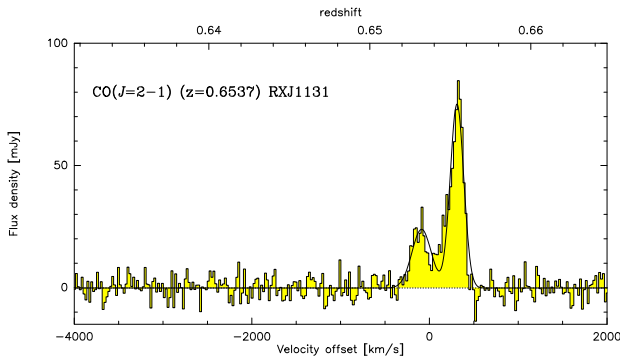

FIG. 1.— Spectrum of CO($J = 2 \to 1$) emission toward RXJ1131. The velocity scale is with respect to z=0.6537, which is approximately the line center considering the asymmetry is as a result of differential lensing. A more detailed discussion of differential lensing effect is presented in §5.1.2 and the magnification factors for various kinematic components are listed in Table 3.

[1] http://hla.stsci.edu/hla_faq.html

We construct the zeroth, first and second moment maps shown in Figure 2 using the *uv*-continuum subtracted data cube, over $\Delta v \sim 750$ km s^{-1}. The first and second moment maps are clipped at 3σ. The peak flux density is 8.12 ± 0.30 Jy km s^{-1} beam^{-1} in the intensity-integrated map. The deconvolved source size is estimated to be $5.''1 \pm 0.''72 \times 3.''72 \pm 0.''66$ and thus the emission is resolved over ~ 2.2 beams. While the lensed emission is not strictly distributed as 2D-Gaussian, the fit recovers the line intensity enclosed within the emitting region, we therefore take this as an estimate on the extent of the lensed emission. On the other hand, if we assume the spatial distribution of the lensed molecular gas emission is similar to that in the optical to near-IR wavelengths, the lensed emission would be more accurately described by an annulus, enclosing the partially complete "Einstein Ring" and the lensed knots (see Figure 2).
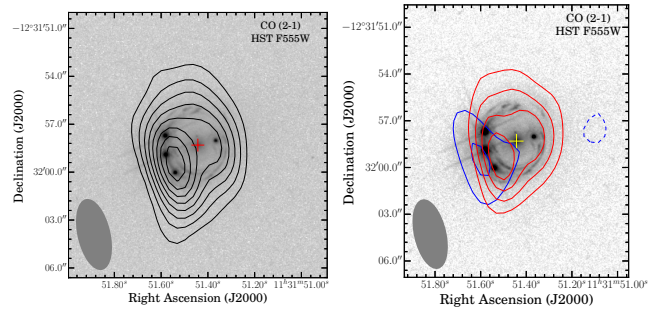

FIG. 2.— Left: an overlay of the velocity-integrated CO($J = 2 \to 1$) emission on the *HST* V–band (F555W) image. Right: contours are color-coded to represent the red and blue wings of the emission. The contours start at 3σ and increment at steps of $\pm 3\sigma$, where $\sigma = 0.3$ mJy beam^{-1}. The crosses denote the location of the foreground galaxy at $z = 0.295$.

The emission of the red component coincides with the Einstein Ring seen in the optical image, with most of its apparent flux originating from the lensed arc in the Southeast, whereas the blue component is predominately coming from solely the lensed arc shown in Figure 2. To illustrate this, we show the channel maps of 21.5 km s^{-1} width and spatial spectra of $1.''5$ resolution in Figure 3 and Figure 4, respectively. The figures show that emission is present to the West, peaking toward the lensing arc (black across in Figure 3) in the red wing, and shifts to the East with decreasing velocity (blue wing). This indicates extended emission in the source plane, where emission from different kinematic components is separated by different amounts relative to the caustics. One consequence of such is the observed asymmetric line profile. A detailed analysis on differential lensing of CO($J = 2 \to 1$) is presented in §5.1.2.

We place an upper limit on HNC($J = 2 \to 1$) line emission at the red-shifted frequency 140 GHz in the foreground galaxy at $z \sim 0.295$) of $\sigma = 1.451$mJy per channel beam^{-1}. Assuming a typical line width of 300 km s^{-1}, this corresponds to a 3σ limit of 4.353 mJy km s^{-1} beam^{-1}.

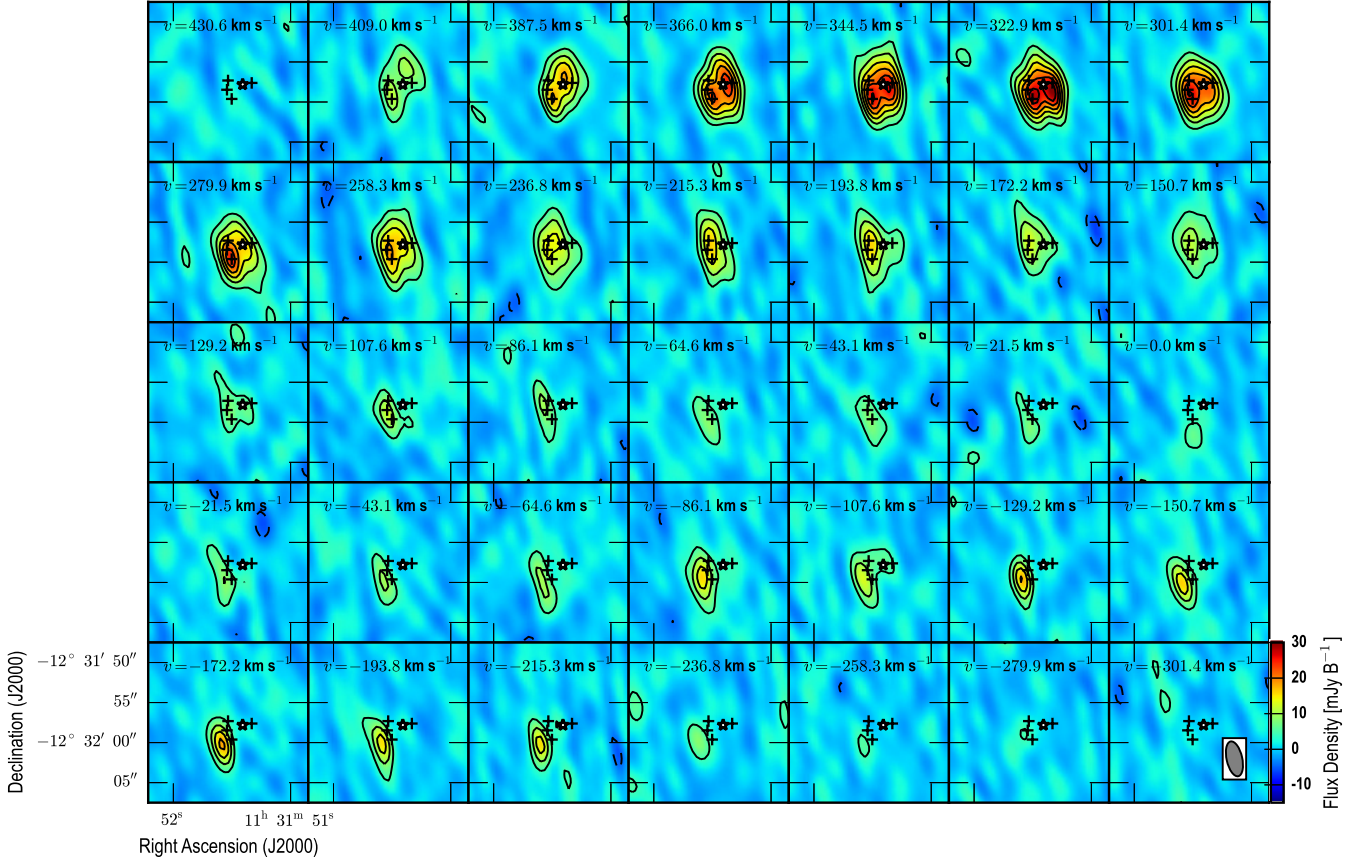### 4.2. *Origin of the CO(J = 2 → 1) Emission*

FIG. 3.— Channel maps of PdBI CO($J = 2 \rightarrow 1$) toward RXJ1131 in 21.5 km s^{-1} resolution. Black crosses indicate the position of the lensed knots (AGN emission, which correspond to components ABCD in C06). The central white-filled star indicates the position of the foreground lensing galaxy (component G in C06). Contours start and increment at steps of $\pm 3\sigma$. The beam is denoted in the bottom right panel.

Evidently, the CO emission is co-spatial with the lensed optical emission in the background AGN host galaxy. The question is then whether the optically faint companion also contributes to the CO flux and thus contains a non-negligible amount of molecular gas. Indeed, based on our lens model presented in §5.1, we find it highly likely that part of the CO emission originates from the companion. We thus classify RXJ1131 as a "wet-wet" merger. However, we cannot quantify this with a mass ratio given the spatial resolution, nor can we rule out the possibility that the "companion" is instead a gas component/tidal feature ripped out from previous interaction. In the subsequent sections, we will interpret the this additional source component as gas emission in a nearby galaxy (i.e. a "wet-wet" merger), as suggested by previous studies of RXJ1131 (C06, B08).

4.3. CO($J = 2 \rightarrow 1$) Kinematics

A clear velocity gradient and an unusually high velocity dispersion ($\gtrsim 400$ km s^{-1}) near the central region is seen in Figure 5. While beam smearing is inevitably the dominant factor in the observed velocity dispersion at the spatial resolution of this data, the exceedingly high velocity dispersion hints at potential perturbations from the AGN, or internal turbulence due to interactions with the companion, and/or instability due to the large gas content. A velocity gradient across the source plane in Figure 8 is also

found in our lens model. This further supports the idea of a kinematically-ordered galaxy, but its emission has been lensed differentially. In this scenario, RXJ1131 is a disrupted disk galaxy hosting an optically bright quasar and is in the process of merging. We will defer the discussion of its implications to §5.2, where we analyze the dynamics of the system in the source plane.

4.4. CO($J = 3 \rightarrow 2$) Emission

We detect resolved CO($J = 3 \rightarrow 2$) line emission toward RXJ1131. The spectrum is shown in Figure 6, which seems to have a double-peak profile. This is expected if RXJ1131 is truly a disk galaxy (see previous sections). The high phase noise in the calibration leads to a low SNR detection. We thus estimate the line intensity to be 35.7 ± 21.9 Jy km s^{-1} by summing up fluxes over the linewidth used to infer CO($J = 2 \rightarrow 1$) line intensity (~ 700 km s^{-1}).

Assuming the spatial extents between CO($J = 2 \rightarrow 1$) and CO($J = 3 \rightarrow 2$) are similar and therefore a negligible differential lensing effect, the line intensities correspond to a brightness temperature ratio of $r_{32} = T_{CO(J = 3 \rightarrow 2)} / T_{CO(J = 2 \rightarrow 1)} = 0.66 \pm 0.41$. The high uncertainty is dominated by the uncertainties in the CO($J = 3 \rightarrow 2$) line intensity.
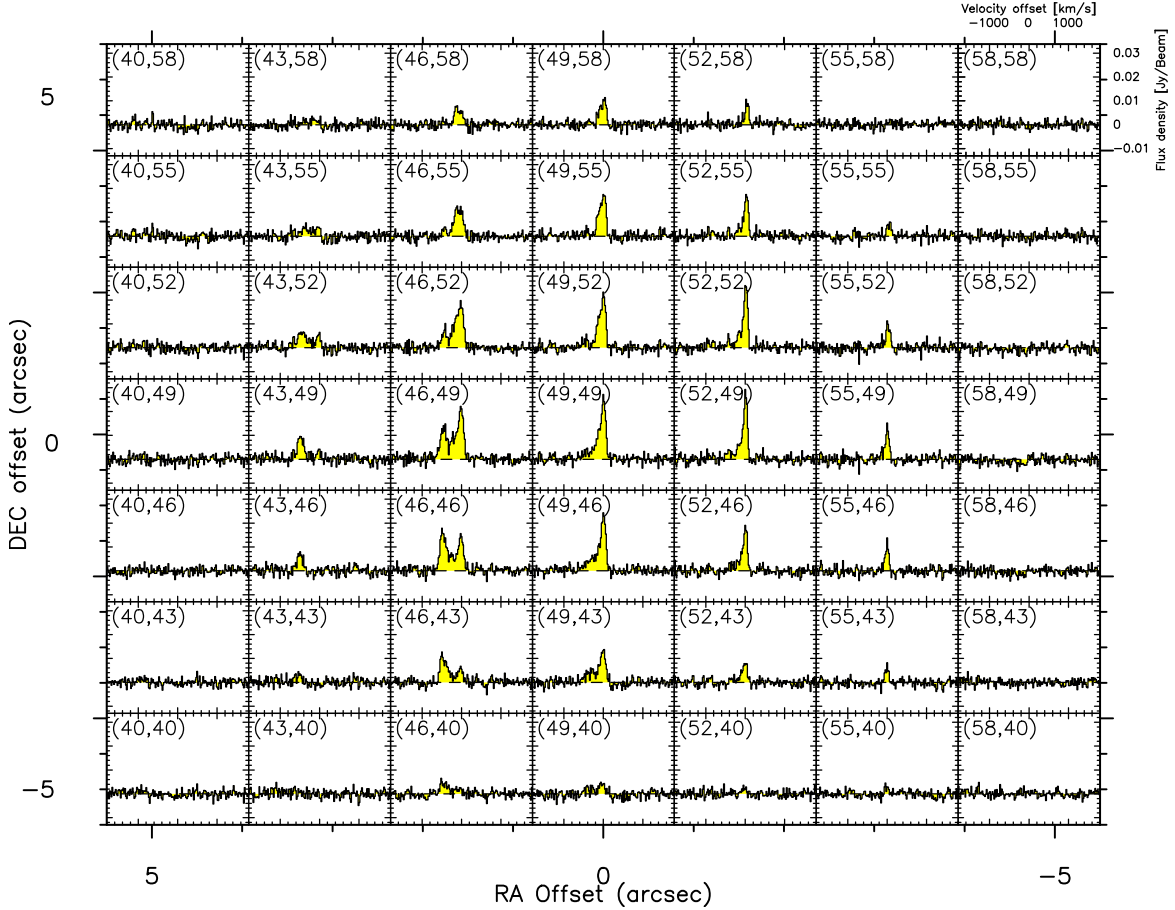
4.5. Interferometric Continuum

FIG. 4.— CO($J = 2 \rightarrow 1$) spectrum as a function of position, binned by 3 pixels in each direction (1″5). The spectra map covers an extent of ~10"×10" centering on the pixel that corresponds to the lensing galaxy. The velocity and flux density scales are denoted in the top right panel. BLAH: DR would want the pixel coordinates replaced by arcsec offset from center.
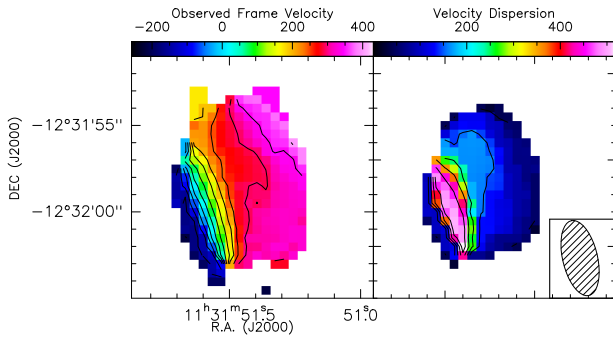

FIG. 5.— Contours for the first (left) and second (right) moment maps are shown in steps of 50 km s^{-1}, and 100 km s^{-1}, respectively. The beam (native resolution) is shown in the right panel.

FIG. 6.— CARMA CO($J = 3 \rightarrow 2$) line profile (solid) without continuum subtraction is over-plotted on the continuum-subtracted CO($J = 2 \rightarrow 1$) line profile (dashed). The velocity scale is with respect to z=0.6537, which corresponds to the dynamical center of the CO($J = 2 \rightarrow 1$) line. The spectral resolution for CO($J = 3 \rightarrow 2$) and CO($J = 2 \rightarrow 1$) is 35.8 km s^{-1} and 21.5 km s^{-1}, respectively.

No 1.5 mm continuum emission is detected at the position of CO($J = 3 \rightarrow 2$) down to a 3σ limit of 2.49mJy beam^{-1}. This is consistent with the spectrum shown in Figure 6.

We detect PdBI 2 mm continuum in Figure 7. The integrated flux density is 1.2 ± 0.2 mJy, with a peak flux $S_\nu = 800 \pm 88$ μmJy beam^{-1} centering on the lensing galaxy. A slightly extended emission is also seen along the lensed arc. This suggests that the detected emission comes from both the foreground galaxy and the background galaxy and that the emission is marginally resolved
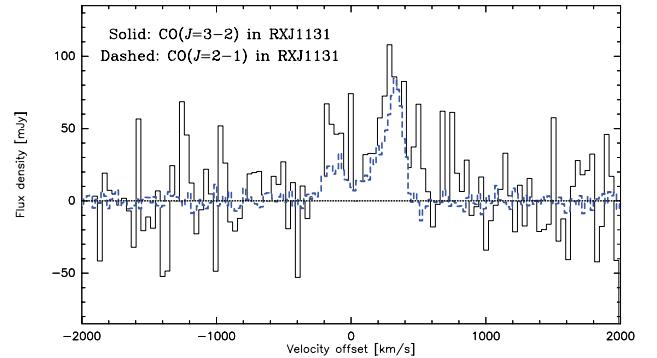
along its major axis. We subtract a point source model in uv-plane to remove the unresolved emission toward the foreground galaxy. The peak flux (0.39 ± 0.08 mJy) in the residual map coincides with the lensed arc, and is consistent with the difference between the integrated and the peak flux in the original continuum map (~0.4 mJy). We therefore adopt $S_\nu = 0.39 \pm 0.08$ mJy as the 2 mm continuum emission toward the background galaxy.

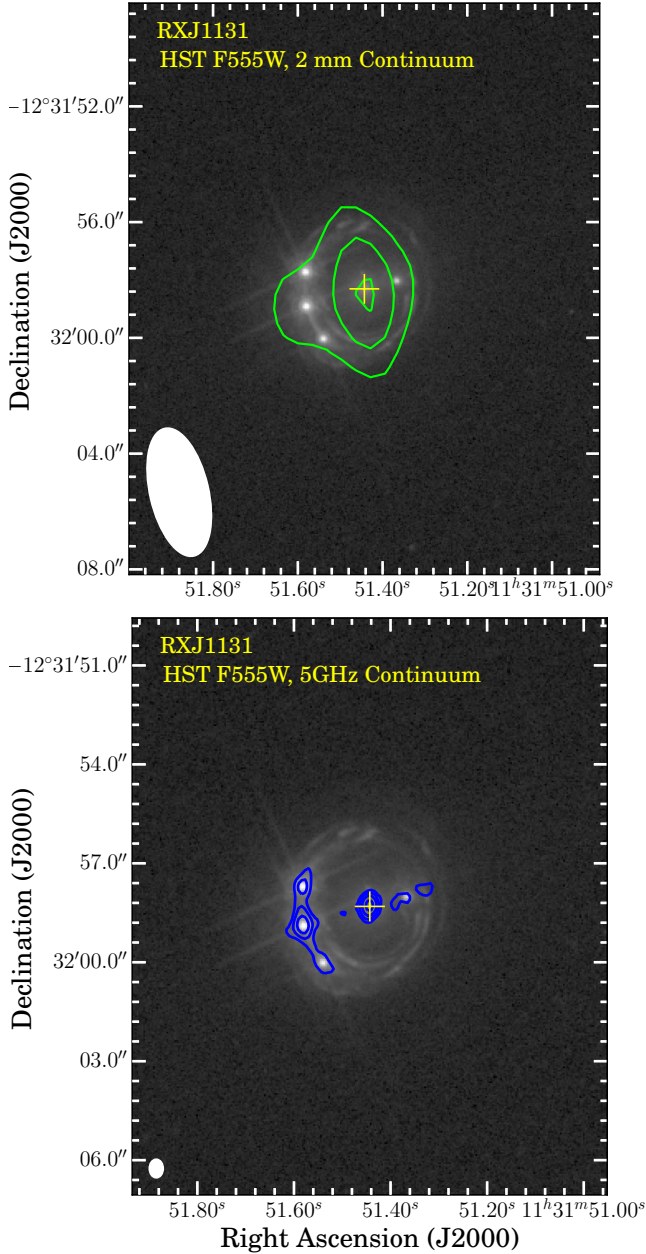The VLA C-band continuum image in Figure 7 shows

FIG. 7.— Top: an overlay of the 2 mm continuum emission on the optical image. Bottom: VLA 5 GHz continuum emission is overlaid on the optical image. Contours in both images start and increment at steps of $\pm 3\sigma$, where $\sigma_{2mm} = 0.082$ mJy beam^{-1} and $\sigma_{5GHz} = 13$ μJy beam^{-1} in the left and right panel, respectively. The central crosses indicate the centroid of the foreground galaxy, as detected in the optical image. The synthesis beams are shown in the bottom left corner of each panel.

resolved emission from the jets and core of the foreground elliptical galaxy as well as emission toward the background quasar. Multiple peaks are seen along the arc and their centroids coincide with the optical emission from the quasar. We extract the flux densities for the arc and the core in Table **??**. We find a spectral index of $\alpha = -0.024$ for the foreground galaxy and $\alpha = -0.345$ for the background galaxy by fitting a power-law ($S_\nu \propto \nu^\alpha$) to the continuum emission at 5 GHz and 2 mm.

4.6. *Photometry*

We compile mid-IR to far-IR broadband photometry (uncorrected for dust extinction) from various catalogs available on the NASA/IPAC Infrared Science Archive (IRSA) in Table **??** with aperture corrections when warranted. These data were obtained from the Two Micron All Sky Survey (2MASS; Skrutskie et al. 2006), Wide-field Infrared Survey Explorer (*WISE*; Wright et al. 2010), *Infrared Astronomical Satellite* (*IRAS*; Neugebauer et al. 1984), and the Multiband Imaging Photometer (MIPS; Rieke et al. 2004) and Mid-infrared Infrared Array Camera (IRAC; Fazio et al. 2004) on *Spitzer Space Observatory*. We retrieve PBCD (level 2) *Spitzer*/IRAC images from the Spitzer Heritage Archive and perform aperture photometry on the channel 1 image to extract flux density at 3.6 μm since it is not available from the IRSA archive.

The emission in the IRAC images is slightly extended. We thus use the *HST* image ($\sim 0\farcs07$ resolution) to determine origins of their centroids, all of which are found to be centered at the position corresponding to the lensed emission from the background galaxy. To recover the diffuse background emission, we subtract a point source model centered on the lensing galaxy, using the average FWHM found by fitting a Gaussian profile to several field stars with the IMEXAM routine of IRAF. We perform aperture photometry on the residual image to obtain decomposed flux measurements from the background galaxy. The photometries for the foreground galaxy are then obtained by subtracting the background emission from the observed total flux. The resulting photometry in Table **??** are obtained after performing aperture correction described in the IRAC Instrument Handbook[2] to correct for the fact that the imaging was calibrated using a 12" aperture, which is bigger than the aperture ($5\farcs8$) we used to perform aperture photometry.

We fit a power-law spectrum to the decomposed IRAC photometry to disentangle the observed total flux at MIPS 24μm. We find a spectral index of $\alpha \sim -1.8$ and $\alpha \sim -0.85$ for the lensing galaxy and RXJ1131, respectively. This is consistent with the mean $3.6 - 8$ μm spectral slope of $\alpha = -1.07 \pm 0.53$ found for unobscured AGN (Stern et al. 2005). An extrapolation of the fit to 24μm yields 33.96 ± 0.01 mJy and 25.19 ± 0.03 mJy for the foreground galaxy and RXJ1131, respectively. We note that the IRAC photometry includes emission from old stellar population and is prone to dust extinction. Hence, the decomposed fluxes are only our best estimate of the warm dust emission. We incorporate the decomposed 24μm point in our SED fitting to provide some constraints on the Wien tail beyond the dust peak of the spectral energy distribution (SED) of RXJ1131. Details of the SED modeling is presented in §5.3.

Extraction of the *Herschel*/SPIRE photometry was carried out using SUSSEXTRACTOR within Herschel Interactive Processing Environment (HIPE; Ott 2010) over the Level 2 maps obtained from the Herschel Science Archive. These maps were processed by the SPIRE pipeline version 13.0 within HIPE. The SUSSEXTRACTOR task estimates

---

[2] http://irsa.ipac.caltech.edu/data/SPITZER/docs/irac/iracinstrumenthandbook/

TABLE 1
PHOTOMETRY DATA

Wavelength micron	Frequency GHz	Flux Density mJy	Instrument
0.555	540167.0	0.056 ± 0.006	HST-ACS/V-Band(L)
0.555	540167.0	0.009 ± 0.0041	HST-ACS/V-Band(H)
0.814	368295.0	0.238 ± 0.013	HST-ACS/I-Band(L)
0.814	368295.0	0.041 ± 0.0054	HST-ACS/I-Band(H)
1.25	239834.0	1.009 ± 0.09	2MASS/J-Band
1.6	187370.0	0.539 ± 0.041	HST-NICMOS(NIC2)/H-Band(L)
1.6	187370.0	0.133 ± 0.004	HST-NICMOS(NIC2)/H-Band(H)
1.65	181692.0	1.448 ± 0.12	2MASS/H-Band
2.17	138153.0	2.064 ± 0.16	2MASS/Ks-Band
3.4	88174.2	7.027 ± 0.14	WISE/W1
3.6	83275.7	5.618 ± 0.0021	Spitzer/IRAC(Extracted)
3.6	83275.7	5.034 ± 0.0021	Spitzer/IRAC(Host)
3.6	83275.7	0.585 ± 0.003	Spitzer/IRAC(Archive-Host)
4.5	66620.5	7.803 ± 0.0021	Spitzer/IRAC(Archive)
4.5	66620.5	6.009 ± 0.0017	Spitzer/IRAC(Host)
4.5	66620.5	1.794 ± 0.0027	Spitzer/IRAC(Archive-Host)
4.6	65172.3	8.872 ± 0.16	WISE/W2
5.8	51688.4	10.720 ± 0.0051	Spitzer/IRAC(Archive)
5.8	51688.4	7.557 ± 0.003	Spitzer/IRAC(Host)
5.8	51688.4	3.163 ± 0.0059	Spitzer/IRAC(Archive-Host)
8.0	37474.1	14.470 ± 0.0041	Spitzer/IRAC(Archive)
8.0	37474.1	9.881 ± 0.0039	Spitzer/IRAC(Host)
8.0	37474.1	4.589 ± 0.0057	Spitzer/IRAC(Archive-Host)
12.0	24982.7	21.960 ± 0.42	WISE/W3
12.0	24982.7	400.000 ± ⋯	IRAS
22.0	13626.9	55.110 ± 1.9	WISE/W4
24.0	12491.4	70.204 ± 0.026	Spitzer/MIPS
25.0	11991.7	500.000 ± ⋯	IRAS
60.0	4996.54	600.000 ± ⋯	IRAS
100.0	2997.92	1000.000 ± ⋯	IRAS
250.0	1199.17	289.427 ± 9.6	Herschel/SPIRE
350.0	856.55	168.229 ± 8.6	Herschel/SPIRE
500.0	599.585	56.782 ± 8.8	Herschel/SPIRE
1387.93	216.0	2.492 ± ⋯	CARMA
2152.82	139.256	1.230 ± 0.22	PdBI-integrated
2152.82	139.256	0.799 ± 0.082	PdBI-peak
2152.82	139.256	0.400 ± 0.082	PdBI-removedFG
61414.0	4.8815	1.273 ± 0.042	VLA/Cband-arc
61414.0	4.8815	0.866 ± 0.027	VLA/Cband-core

REFERENCES. — blah

NOTE. — blah

the flux density from an image convolved with a kernel derived from the SPIRE beam. The flux density measured by SUSSEXTRACTOR is additionally confirmed using the Timeline Fitter, which performs photometry by fitting a 2D elliptical Gaussian to the Level 1 data at the source position given by the output of SUSSEXTRACTOR.

5. ANALYSIS

5.1. *Lens modeling*

At the angular resolution of the CO($J = 2 \rightarrow 1$) data, the images are resolved but not within the multiply lensed emission (i.e., sub-optimal for performing lens modeling). Nevertheless, the high spectral resolution of this data provides dynamical information on spatial scales smaller than the beam (see Figure 5). Hence, with the high SNR, we reconstruct the intrinsic gas dynamics by carrying out a parametric lens modeling over different channel slices of the interferometric data using our lensing code UVMCMC-FIT (Bussmann et al. 2015; see Bussmann et al. 2015 for details of the code). Model of each slice in Figure 8 thus provides properties on the intrinsic kinematics. The slices are obtained by binning the data over the full linewidth

TABLE 2
LENS PARAMETERS FROM PRELIMINARY MODELS

Parameters		Median values
Offset in RA	($''$)	0.004±0.027
Offset in Dec	($''$)	0.003±0.027
Axial Ratio		0.56±0.16
Position Angle	(deg)	103±22
Einstein Radius	($''$)	1.833±0.002

NOTE. — Parameters describing the foreground lens are obtained based on the preliminary models (see text for details). All angular offsets are with respect to $\alpha = 11^h31^m51\overset{s}{.}44$, $\delta = -12°31'58\overset{''}{.}3$ (J2000).

$\sim$700 km s^{-1} by five channels, that is, into seven slices, to increase the SNR.

The lens mass distribution is modeled using a singular isothermal ellipsoid (SIE) profile, which is described by five free parameters: the positional offset in R.A. and Dec. relative to an arbitrary chosen fixed coordinate in the image, the Einstein Radius, the axial ratio, and the position angle. We use the VLA radio continuum emission toward the foreground galaxy to initialize the positional offset. We impose a uniform prior ±0$\overset{''}{.}$05 in both ΔR.A. and ΔDec., motivated by the astrometry uncertainties in the VLA image as well as the uncertainties provided by previous SIE lens model (C06). We initialize the Einstein Radius based on the model parameters reported by C06 and impose a uniform prior using ±3σ of their uncertainties. The sources are modeled using elliptical Gaussian profiles, which are parameterized by six free parameters: the positional offset in R.A. and Dec. relative to the lens, the intrinsic flux density, the effective radius, the axial ratio, and the position angle. The position of each source is allowed to vary between ±1$\overset{''}{.}$5 (i.e., within the Einstein Radius) and the effective radius is allowed to vary from 0$\overset{''}{.}$01−2$''$.

Our code uses an Markov Chain Monte Carlo (MCMC) approach to sample the posterior probability distribution function (PDF). In each model, we require a target acceptance rate of $\sim$0.25−0.5 and check for chain convergence by inspecting trace plots and requiring the samples are beyond at least an autocorrelation time. We thus employ $\sim$50,000 samples as the initial "burn-in" phase to stabilize the Markov chains (which we then discard) and use the final $\sim$5,000 steps, sampled by 128 walkers, to identify the posterior. Here, we identify the best-fit model and the quoted uncertainties using the median and the 68% confidence intervals in the marginal PDFs.

We first obtain a preliminary lens model for each channel slice independently, where their lens parameters are allowed to vary and are initialized according to the aforementioned way. We obtain the final model by repeating the modeling over each slice but fixing their lens parameters according to the overall median in the preliminary models, as listed in Table 2. This ensures that all models share the same lens profile. The magnification factors in Table 3 are determined by taking the ratio between the image plane flux and the source plane flux of each model.

TABLE 3
MAGNIFICATION FACTORS OF VARIOUS
KINEMATIC COMPONENTS IN CO($J = 2 \rightarrow 1$)

Channel	Source 1 μ_L	Source 2 μ_L
126–130	7.2 ± 5.6	6.7 ± 2.5
131–135	7.6 ± 1.6	
136–140	8.7 ± 2.0	
141–145	4.1 ± 0.9	
146–150	4.2 ± 0.6	
151–155	4.3 ± 2.4	
156–160	3.1 ± 0.9	
weighted average	4.4	
median	5.5	

NOTE. — Source 1 is RXJ1131 and source 2 is its companion. See text for details.

Our model parameters in Table 2, describing the mass distribution of the lensing galaxy, are consistent (within the uncertainties) with that of the SIE model presented by C06. We find a mass of $M(\theta < \theta_E) = (7.47 \pm 0.02) \times 10^{11} M_\odot$ within the Einstein radius.

5.1.1. *Interpretation and Caveats*

The reconstructed source locations in Figure 8 demonstrate an intrinsic velocity gradient across the source plane, which is indicative of a disk-like galaxy. While solely based on the lens model is insufficient to draw conclusive inference on its true geometry. Additional support to the disk conjecture can be found in the double-horned line profile (Figure 1) and the observed (image plane) velocity field (Figure 5). Furthermore, C06 also find that the reconstructed source plane emission in optical-NIR is best-reproduced using a $n = 1$ Sersic profile. Our interpretation therefore tends in favor of a disk morphology for RXJ1131.

One other interesting result from our lens model is that a better fit is found for the red-most channel if we add a second source component (see top left panel in Figure 8). This is consistent with previous results reported by Brewer & Lewis (2008), who find an optically faint companion (component F in their paper) ~ 2.4 kpc away from the AGN host galaxy, and C06, who find evidence for an interacting dusty galaxy. Spatially, the red velocity component of the CO also coincides with this component F. While we cannot quantify the type of merger (major v.s. minor) with a mass ratio given the spatial resolution, the symmetric velocity gradient retained under such close separation between the two lean support to the idea of a minor merger.

We emphasize that the spatial resolution of the data in hand is a few arcsec, which implies that despite the high SNR and spectral resolution, this data is insufficient to constrain the intrinsic sizes of the lensed galaxies, and thus the magnification factors are likely under-predicted. We will discuss this further in the following section.

5.1.2. *Differential Lensing*

Previous lens models of RXJ1131 find evidence for differential lensing across *HST H-*, *V-*, and *I*-band (C06),

where the magnification factor ranges from 10.9 to 7.8. C06 attribute the decrease toward the IR regime is caused by the more extended IR emission. The highly asymmetric CO($J = 2 \rightarrow 1$) line profile suggests that differential lensing is also non-negligible for CO, where the redshifted emission is apparently much brighter than that in the blueshifted part, consistent with the source positions relative to the caustics in Figure 8. The red wing emission mainly originates near the cusp in the caustic, whereas the blue wing emission is located beyond the caustics. The magnification factor for CO ranges from 8.7 to 3.1 (Table 3).

5.2. *CO($J = 2 \rightarrow 1$) Dynamical modeling*

This section proceeds under the assumption that RXJ1131 is a rotating disk (see previous sections). Assuming the velocities of the respective channels used in lens modeling correspond to solely the tangential component of the true velocity vector (i.e., along the major axis), we extract a one dimensional PV diagram in Figure 9 by slicing across their source plane positions (PA: 121°).

We attempt to characterize the molecular gas kinematics using an empirically-motivated disk model (e.g., Courteau 1997; Puech et al. 2008; Miller et al. 2011):

$$V = V_0 + \frac{2}{\pi} V_a \arctan(\frac{R}{R_t}), \qquad (1)$$

where V is the observed velocity, V_0 is the velocity at dynamical center, V_a is the asymptotic velocity, and R_t is the "turnover" radius at which the rotation curve becomes flat. We perform non-linear least square fitting using an orthogonal distance regression to find the best-fit parameters, taking into account the uncertainties in both velocity (channel width) and distance offset. We also place an upper limit on $R_t < 15$ kpc to keep this parameter physical (e.g., Puech et al. 2008; Miller et al. 2011). The parameter uncertainties are inferred based on Monte Carlo simulation of 500 iterations, where the input parameters are perturbed according to random Gaussian distributions of sigmas corresponding to their uncertainties. Using this model, we find $V_a = 975 \pm 387$ km s^{-1}, $R_t = 10.6 \pm 5.7$ kpc, and $V_0 = 28 \pm 40$ km s^{-1}. We note, however, that since emission is not detected beyond the flat regime of the rotation curve, the asymptotic velocity is poorly constrained and the "turnover" radius is at most a lower limit. In particular, V_a and R_t are highly correlated with a Pearson coefficient $R = 0.998$, and 0.027 between V_a and V_0.

We note that the asymptotic velocity (V_a) – an extrapolation of the model out to radius beyond the disk scale-length and half-light radius – is inequivalent to maximum observed velocity (V_{max}), which is commonly used in literature to parameterize disc rotation. The arctangent model is most commonly used in studies of the Tully-Fisher relation, where an extrapolation to $V_{2.2}$ (velocity at 2.2 disc scale-length or ~ 1.375 half-light radius, or $\sim 0.7 R_{opt}$[3]) is typically adopted as the rotation velocity (V_{max} in their terminology) since this corresponds to the radius at which the
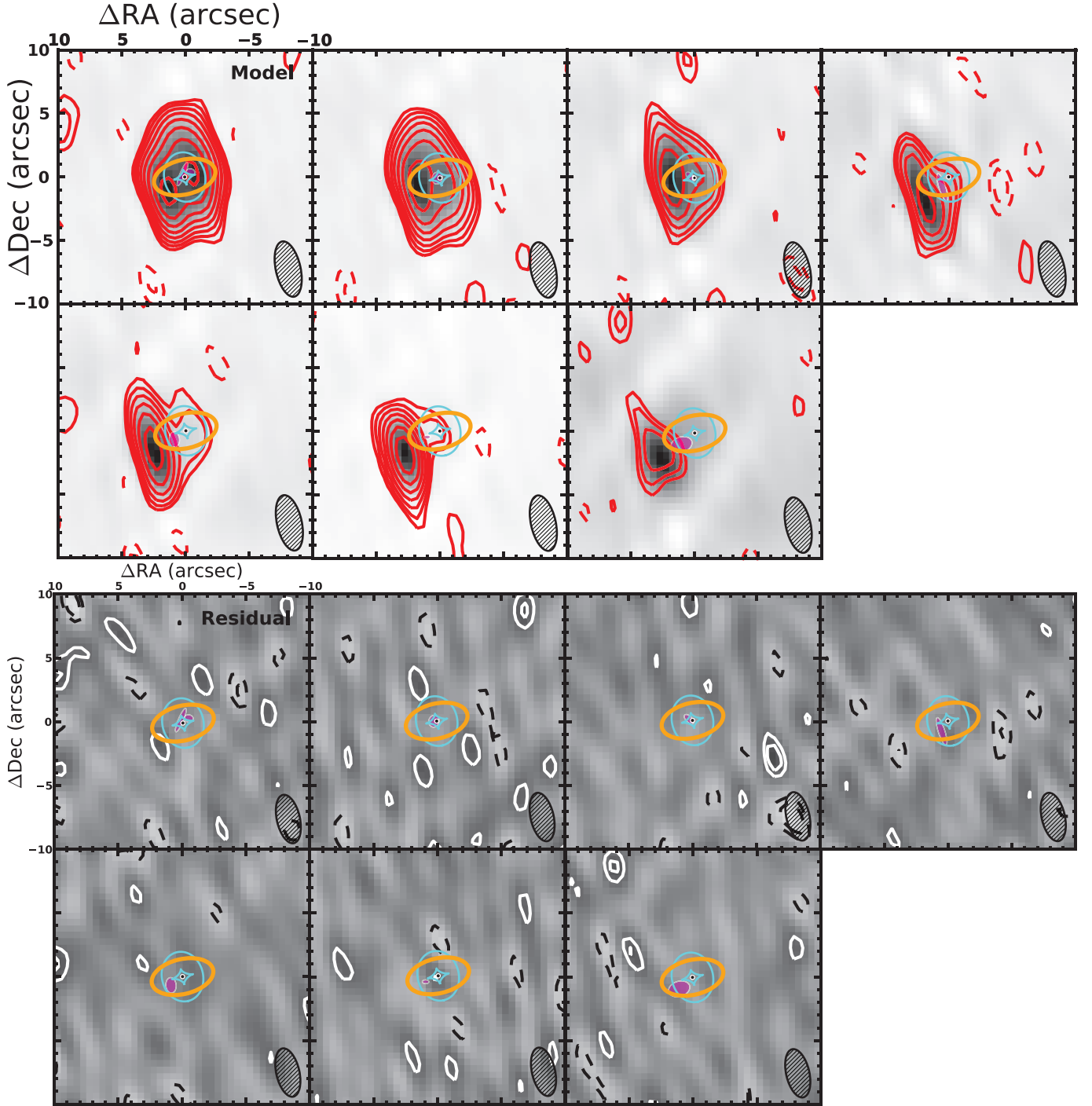
---

[3] Radius enclosing 83% of the light distribution.

FIG. 8.— Each panel corresponds to a lens model of RXJ1131 performed over a channel slice ∼100 km s^{-1} of the CO($J = 2 \rightarrow 1$) data. Top: channel maps of the PdBI CO($J = 2 \rightarrow 1$) emission (red) overlaid on our best-fit lens models (grayscale). The location of the foreground lensing galaxy is indicated by a black dot and its critical curve is traced by the orange solid line. The locations and morphologies (half-light radii) of the reconstructed sources are represented by magenta ellipses (see text in §5.1.1 for caveats). The caustic curves are represented as cyan lines. The beam of the PdBI observations is shown in the bottom right corner of each panel. Bottom: residual images of the best-fit models, obtained by taking the Fourier transform after subtracting the best-fit model from the data in the uv-domain. Contours start at ±3σ and increment at steps of $3 \times 2^n \sigma$, where n is a positive integer.
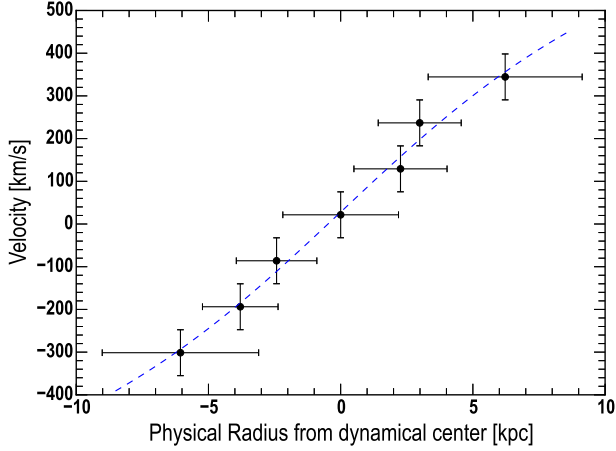
FIG. 9.— PV slice along the major axis in the source plane at PA = 121°. Dashed line shows the best-fit rotation curve using an arctangent model. The vertical error bars show the channel width for each model and the horizontal error bars are the 1σ uncertainties on the source plane positions. DR may suggest include 68& fits from MC simulation, maybe I will do that later.

velocity of a pure exponential disc peaks. We here adopt the maximum *observed* velocity $V_{rot} = 345 \pm 55$ km s^{-1} at 6 ± 3 kpc from the dynamical center as a proxy to the rotation velocity. This radius corresponds to $\sim 0.6 R_e$, where R_e is the half-light radius ~ 10.3 kpc inferred from the *HST* *I*-band lens model (C06; converted to our cosmology). We note that the source plane half-light radius varies substantially with wavelength. In particular, the half-light radius is found to be ~ 4 kpc and ~ 7 kpc in *V*-band (Brewer & Lewis 2008) and *H*-band (C06), respectively. This discrepancy arises owing to the exclusion of the more diffused emission in *V*-band (rest-frame UV), which traces young massive stars. The *V*-band compactness may be explained in part due to the fact that its emission is more susceptible to dust extinction than other bands. On the other hand, the molecular gas (fuel for star-formation) is more compact than the more evolved stellar population, as traced by *I* and *H*-bands. This is consistent with the picture that stars diffuse outward after their formation (Calzetti 2001).

Using the V_{rot} from last paragraph, we find a dynamical mass of $M_{dyn} \sin^2 i (< 6 \,\text{kpc}) = 17 \times 10^{10}\,M_\odot$ enclosed within the CO-emitting region. If we instead consider the line peak separation from the CO($J = 2 \to 1$) line profile $\Delta v_{sep}/2 \sim 110$ km s^{-1}, we find $M_{dyn} \sin^2 i (< 6 \,\text{kpc}) = 1.8 \times 10^{10}\,M_\odot$. **DR: here, I list the extrema for possible Mdyn given our data, should I say anything more?** We correct for the inclination effect using the morphological axial ratio from the reconstructed image (Figure 3 in C06), where the minor axis is $1''8$ and the major axis is $3''25$. We thus find an inclination angle of 56.4°, which is consistent with the observed unobscured AGN and an observable double peak line profile. The dynamical mass is then $2.5 \times 10^{10} M_\odot < M_{dyn} (< 6\,\text{kpc}) < 25 \times 10^{10} M_\odot$. Since this quantity is derived under the assumption that the gas is virialized, which is highly unlikely given the velocity dispersion and the presence of a close companion, our estimate is at most a lower limit. We caution that this analysis is based on limited spatial resolution data and will be

TABLE 4
SED FITTING RESULTS

Parameters		With 24μm	Without 24μm
T_d	(K)	$52.0^{+4.0}_{-4.1}$	$58.2^{+14.5}_{-14.4}$
β		$1.8^{+0.5}_{-0.6}$	$2.1^{+0.3}_{-0.3}$
α		$1.6^{+0.5}_{-0.5}$	$8.9^{+6.9}_{-6.3}$
λ_0 [a]	(μm)	548^{+285}_{-307}	367^{+125}_{-145}
λ_{peak} [b]	(μm)	162^{+16}_{-30}	146^{+39}_{-44}
$f_{\text{norm}, 500\mu\text{m}}$ [c]	(mJy)	59^{+14}_{-13}	60^{+5}_{-5}
L_{FIR} [d]	($10^{12} L_\odot$)	$3.81^{+2.04}_{-1.92}$	$4.72^{+2.54}_{-2.26}$
M_d [e]	($10^8 M_\odot$)	22^{+5}_{-18}	11^{+5}_{-6}

NOTE. — Errors reported here are $\pm 1\sigma$. L_{FIR} and M_d are not corrected for lensing.

[a] Observed-frame wavelength where $\tau_\nu = 1$
[b] Observed-frame wavelength of the SED peak
[c] Observed-frame flux density at 500 μm
[d] Rest-frame 42.5–122.5 μm luminosity
[e] Derived assuming absorption mass coefficient of $\kappa = 2.64$ m^2 kg^{-1} at $\lambda = 125.0$ μm (Dunne et al. 2003)

verified with future higher-resolution observations.

5.3. *SED modeling*

We fit dust SED models to the 24 μm−2.2 mm photometry in Figure 10, where we also include the IRAS 60 μm and 100 μm upper limits to constrain the dust peak. The fit is performed with the code MBB_EMCEE (e.g., Dowell et al. 2014), which samples the posterior using an MCMC approach and uses instrumental response curves to perform color correction on-the-fly. The SED model consists of a modified-blackbody function with a power-law attached to the Wien side to account for an excess in the MIR owing to warm, small dust emission. The model is thus described by five free parameters: the rest-frame characteristic dust temperature (T_d), the emissivity index (β), the power-law index (α), the flux normalization at 500 μm (f_{norm}), and the observed-frame wavelength at which the emission becomes optically thick (λ_0). We impose an upper limit of 100 K on T_d, a Gaussian prior centered around $\mu = 1.9$ with $\sigma = 0.3$ on β, and an upper limit of 1000 μm on λ_0. We check for chain convergence by requiring the autocorrelation length of each parameter to be less than the number of steps taken for the burn-in phase (which are then discarded). Here we report the modes and the 1σ confidence intervals in the marginal PDFs as the best-fit parameters, as listed in Table 4.

In the first model, we include the 24 μm data to constrain the power-law index. Based on the best-fit of this model, we find a far-IR luminosity (rest-frame 42.5 − 122.5 μm) of $3.81^{+2.04}_{-1.92} \times 10^{12} L_\odot$ and a dust mass of $22^{+5}_{-18} \times 10^8 M_\odot$. For the mass absorption coefficient, we adopt $\kappa = 2.64$ m^{2}kg^{-1} at 125.0 μm (rest frame; Dunne et al. 2003). The dust mass uncertainty does not include those in the absorption coefficient. These values are not corrected for lensing.

A fit including the MIR 24 μm photometry is likely an upper limit on the far-IR luminosity arising from starburst. If we instead fit for a model excluding the 24 μm con-

straint, two major consequences are immediately apparent. First, the power-law index is poorly-constrained (see Table 4). Second, the steep power-law implies a small contribution from the power-law regime to the total IR luminosity as compared to the graybody. Thus, the far-IR luminosity in this model should, in principle, corresponds to a lower limit on the cold dust emission. Using the best-fit parameters for this model, we find a total IR luminosity $L_{\rm IR}$ (rest-frame $8-1000\,\mu$m) of $8.14^{+2.64}_{-2.80}\times10^{12}\,L_\odot$, a far-IR luminosity $L_{\rm FIR}$ of $4.72^{+2.54}_{-2.26}\times10^{12}\,L_\odot$ and a dust mass ($M_{\rm dust}$) of $11^{+5}_{-6}\times10^8\,M_\odot$. Taken at face value, this implies a $L_{\rm FIR}$-to-$L_{\rm IR}$ contribution of $\sim$58%. Again, the inferred quantities are uncorrected for lensing.

The dust temperature from both models is similar to that of ULIRGs at $0.6 < z < 1.0$ (54 ± 5 K; Combes et al. 2013, hereafter C13). We note the far-IR luminosity is comparable in both models, which is not surprising given the lack of constraints in the MIR. In fact, the far-IR luminosity from the second model is slightly higher than the former, but consistent within the uncertainties. For the subsequent analysis, we adopt the physical quantities from the former (i.e., with constraints at $24\,\mu$m). The choice of SED model does not affect the derived star formation rate (SFR) given the similar far-IR luminosity. Yet, the dust mass is higher in the former (but consistent within the uncertainties), and thus the gas-to-dust ratio in §5.4 should be considered as an estimate. We correct for lensing using the median magnification factor ($\mu_{\rm L} = 5.5$) from the CO lens models. This yields a $L_{\rm FIR}$ of $(6.9\pm3.6)\times10^{11}\,L_\odot$. Assuming a Salpeter initial mass function (Salpeter 1955), we find a SFR of $(120\pm63)\,M_\odot$ yr^{-1} using the standard conversion (Kennicutt 1998).
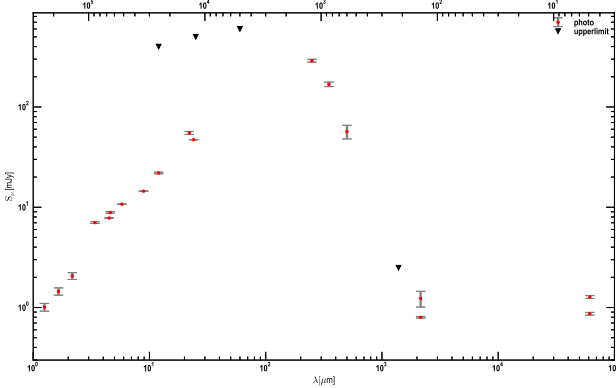

FIG. 10.— SED models of the IR dust emission toward RXJ1131. The data are not corrected for lensing magnification and dust extinction. **This figure needs an update** WISE flux is slightly higher than the IRAC point, probably due to a smaller aperture used in IRAC extraction, both of which were taken from the archive. IRAC: Aperture flux in 5$''$diameter. MIPS: use PSF fit flux from archive as source size < PSF FWHM of 6$''$. Might want to add NVSS constraints.

To place RXJ1131 in context of existing studies, we compare its properties with those reported by C13, which is the largest sample of IR-luminous galaxy at similar redshift ($0.6 < z < 1.0$) with CO measurements. Since C13 adopt a different definition of $L_{\rm FIR}$ ($40-500\,\mu$m)[4], we

derive the far-IR luminosity following this convention. This yields $(8.8\pm0.4)\times10^{11}(\mu_{\rm L}/5.5)\,L_\odot$ and a SFR of $(150\pm70)\,M_\odot$ yr^{-1}. This implies that RXJ1131 is considered a LIRG in regard to their sample, and consequently, the SFR of RXJ1131 is lower (cf. SFR > 200, with an average of 1200 in C13). If we instead adopt the more generally used definition for the total IR luminosity ($L_{\rm IR} > 10^{12}$), RXJ1131 would be considered a ULIRG given its lensing-corrected total IR luminosity of $\sim2\times10^{12}\,L_\odot$.

5.4. *Gas properties*

In this section, we derive the gas properties of RXJ1131 based on CO($J = 2 \to 1$), and compare the derived quantities against those reported by C13, where their results are based on CO($J = 2 \to 1$) and CO($J = 4 \to 3$) line observations on the IRAM 30-m dish.

5.4.1. *Linewidth & Sizes*

We find that the linewidths for both components (redshifted and blueshifted) inferred from a double Gaussian fit to the line profile are comparable to the C13 ULIRG sample ($\Delta v_{\rm FWHM}$ of $370\,{\rm km\,s^{-1}}$) and local ULIRGs ($300\pm85\,{\rm km\,s^{-1}}$; Solomon et al. 1997). Since C13 do not have resolved observations, we compare the gas distribution with local U/LIRGs. The CO gas in RXJ1131 is distributed $\sim$6 kpc in radius across (in the source plane), which is more extended than the sample of disk-like U/LIRGs studied by Ueda et al. (2014, hereafter U14), who find an average radius of 3.5 ± 2.3 kpc with a range spanning $1.1-9.3$ kpc.

5.4.2. *Gas Mass*

To derive the molecular gas mass, we first correct for lensing magnification using the respective magnification factors listed in Table 3, which to first order takes into account effect of differential lensing. This yields $I_{\rm CO(J=2\to1)} = 5.9\pm2.7$ Jy km s^{-1}, where the uncertainty includes those on the magnification factors. We note that this includes emission from the companion as the spatial resolution of our data do not allow us decompose its contribution from the total line flux.

Without direct CO($J = 1 \to 0$) measurements, we derive CO($J = 1 \to 0$) intensity using a brightness temperature ratio of $r_{32} = 1$, which was chosen solely to facilitate a comparison with other U/LIRGs. For the same reason, we adopt a luminosity-to-mass conversion factor of $\alpha_{\rm CO} = 0.8$ (K km s^{-1} pc^2)$^{-1}$, this yields a CO luminosity $L'_{\rm CO} = (3.47\pm1.58)\times10^{10}$ K km s^{-1} pc^2 and a gas mass $M_{\rm gas}$ of $(2.8\pm1.3)\times10^{10}\,M_\odot$. This is likely an overestimation for RXJ1131 due to a contribution from the companion. The inferred gas mass is comparable to C13 sample ($M_{\rm gas} = 1.5\times10^{10}M_\odot$) as well as local U/LIRGs (Solomon et al. 1997; Sanders & Mirabel 1996) but higher than local LIRGs (U14).

We place a lower limit on the dynamical mass (see §5.2) using the inferred gas mass. This BLAH. **will need**

---

[4] We also note that the far-IR luminosity in C13 is derived based on 60$\,\mu$m

and 100$\,\mu$m IRAS fluxes.

edit depending on the dyn. modeling section a gas-to-dynamical mass fraction of $f_{\text{gas–dyn}} = \text{BLAH}$. Using the dust mass derived from SED fitting, we find a gas-to-dust ratio of 184 ± 124, which is consistent with the C13 sample ($f_{\text{gas–dust}} = 206$) and local U/LIRGs (200–350; Sanders et al. 1991, Contini & Contini 2003; Seaquist et al. 2004; Wilson et al. 2008).

5.4.3. *SFE and Depletion Time*

We derive the SFE using the far-IR luminosity definition used by C13 (i.e., $\text{SFE} \pm L_{\text{FIR}} \, (40-500 \, \mu\text{m})/M_{\text{gas}}$), we find a SFE of 31 ± 15 for RXJ1131, or equivalently a depletion timescale of $\tau = 190 \pm 70$ Myr. This SFE is substantially lower than most U/LIRGs (Solomon et al. 1997; Combes et al. 2011; C13). **am I doing something wrong...**

Implication of this unexpectedly low SFE in RXJ1131...

6. DISCUSSION

6.1. *Merger stage of RXJ1131-1231*

In this section, we put our results in context with other ULIRGs/mergers at $z = 0 - 1$. It is clear that RXJ1131 has a gas-rich companion, but how does this affect its internal dynamics? What is the merger stage of RXJ1131? We argued that the symmetric source-plane velocity field suggest the system is a minor merger, consistent with an earlier study by B08, who independently conclude that the companion is likely a dwarf of size ~ 700 kpc across.

While our result is consistent with other studies of RXJ1131, it contrast strongly with studies of local (U)LIRGs/mergers ($L_{\text{IR}} = 10^{11-12.5} \, L_\odot$; $z < 0.1$), where AGNs are typically found in late stage mergers (Yuan et al. 2010; Iwasawa et al. 2011; Carpineti et al. 2012) and that only these major mergers near their final coalescence can provide $L_{\text{IR}} > 10^{12} \, L_\odot$, (e.g., Carpineti et al. 2015; Larson et al. 2016, hereafter L16) [5]. If this is also the case at $z \sim 0.65$, it would imply RXJ1131 is a major merger near its final coalescence and that the spatially offset component is likely an expulsion of gas driven by AGN winds or some tidally ejected material from previous passage. In that case, the molecular gas fraction in the host galaxy should have declined (as seen in ellipticals) compared to early stage mergers **can we find molecular gas mass fraction as a function of merger stage? also, what is the dynamical mass for RXJ1131** and that the molecular gas would be more concentrated in the nuclear region. This is inconsistent with what is observed for RXJ1131 (an extended gas-rich disk; but see also U14 for outliers with extended molecular gas in merger remnants) and the fact that there is on-going star-formation activity. Hence, we

reject this and speculate the discrepancy is a consequence of different power mechanisms of IR-luminous galaxies at intermediate redshift.

An alternative explanation might be that the CO is less strongly-magnified as compared to the dust emission, in which case, the lensing-corrected IR luminosity is overestimated. This is plausible given the extent of the source with respect to the caustics and that substantial differential lensing effect has been seen across CO and other wavelengths. If we instead use the NIR (*H*-band) magnification factor ($\mu_L = \text{BLAH}$; C06), we find $L_{\text{FIR}} = \text{BLAH}$. This would imply that RXJ1131 is a large gas-rich LIRG, and a minor merger in the context of the results reported by Carpineti et al. (2015) and L16.

— anything below is not ready —

6.1.1. *Fate of RXJ1131-1231*

Has RXJ1131 encountered with the companion?

From numerical simulations, mergers are observable and distinguishable with their kinematic and morphological features for 0.2–0.4 Gyr between their second passage and final coalescence.

The spinning black hole in RXJ1131 provide one piece of evidence that the two has already encountered.

Mergers are expected to evolve into local ellipticals or large-disks (bulge dominated) (springel & Hernquist 05, cite). Given the extended molecular gas distribution, we suggest RXJ1131 may evolve into the latter (large-disk) unless the "companion" BKAH SOME STUFF or some other mechanisms at play in the latter stage, transporting the gas toward the central nuclear region and blah.

6.2. *ULIRG Evolution and Cosmic SFH*

While there is an emerging consensus on the strong evolution of the IR luminosity function (e.g., Huynh et al. 2007; Seymour et al. 2010), it is currently unclear whether the IR luminosity of these intermediate redshift sources arise due to the merging of large spiral galaxies, as typically seen in local ULIRGs, or proceed under a different formation processes at higher redshifts. Our study blah...

Our result indicates that...

7. SUMMARY AND CONCLUSIONS

We investigate the cold gas kinematics and dynamics in the lensed optical quasar RXJ1131 at $z_{\text{CO}} \sim 0.65$ by observing its CO($J = 2 \rightarrow 1$) and CO($J = 3 \rightarrow 2$) line emission. Our results suggest that RXJ1131 is a wet-wet merger between an AGN/starburst ULIRG and a optically faint companion.

Brewer, B. J., & Lewis, G. F. 2008, MNRAS, 390, 39
Bussmann, R. S., Riechers, D., Fialkov, A., et al. 2015, ApJ, 812, 43

Bussmann, S., Leung, T. K. D., & Conley, A. 2015, uvmcmcfit
Calzetti, D. 2001, PASP, 113, 1449
Carpineti, A., Kaviraj, S., Darg, D., et al. 2012, MNRAS, 420, 2139
Carpineti, A., Kaviraj, S., Hyde, A. K., et al. 2015, A&A, 577, A119

[5] In this section, we adopt the total IR luminosity calculated from $8 - 1000 \, \mu$mto be consistent with the classification used by these authors.

Combes, F., García-Burillo, S., Braine, J., et al. 2011, A&A, 528, A124

—. 2013, A&A, 550, A41

Courteau, S. 1997, AJ, 114, 2402

Dowell, C. D., Conley, A., Glenn, J., et al. 2014, ApJ, 780, 75

Dunne, L., Eales, S. A., & Edmunds, M. G. 2003, MNRAS, 341, 589

Fazio, G. G., Hora, J. L., Allen, L. E., et al. 2004, ApJS, 154, 10

Hinshaw, G., Larson, D., Komatsu, E., et al. 2013, ApJS, 208, 19

Huynh, M. T., Frayer, D. T., Mobasher, B., et al. 2007, ApJ, 667, L9

Iwasawa, K., Sanders, D. B., Teng, S. H., et al. 2011, A&A, 529, A106

Kennicutt, Jr., R. C. 1998, ARA&A, 36, 189

Larson, K. L., Sanders, D. B., Barnes, J. E., et al. 2016, ArXiv e-prints, arXiv:1605.05417

Miller, S. H., Bundy, K., Sullivan, M., Ellis, R. S., & Treu, T. 2011, ApJ, 741, 115

Neugebauer, G., Habing, H. J., van Duinen, R., et al. 1984, ApJ, 278, L1

Ott, S. 2010, in Astronomical Society of the Pacific Conference Series, Vol. 434, Astronomical Data Analysis Software and Systems XIX, ed. Y. Mizumoto, K.-I. Morita, & M. Ohishi, 139

Puech, M., Flores, H., Hammer, F., et al. 2008, A&A, 484, 173

Rieke, G. H., Young, E. T., Engelbracht, C. W., et al. 2004, ApJS, 154, 25

Salpeter, E. E. 1955, ApJ, 121, 161

Sanders, D. B., & Mirabel, I. F. 1996, ARA&A, 34, 749

Sanders, D. B., Scoville, N. Z., & Soifer, B. T. 1991, ApJ, 370, 158

Seymour, N., Symeonidis, M., Page, M. J., et al. 2010, MNRAS, 402, 2666

Skrutskie, M. F., Cutri, R. M., Stiening, R., et al. 2006, AJ, 131, 1163

Solomon, P. M., Downes, D., Radford, S. J. E., & Barrett, J. W. 1997, ApJ, 478, 144

Stern, D., Eisenhardt, P., Gorjian, V., et al. 2005, ApJ, 631, 163

Ueda, J., Iono, D., Yun, M. S., et al. 2014, ApJS, 214, 1

Wright, E. L., Eisenhardt, P. R. M., Mainzer, A. K., et al. 2010, AJ, 140, 1868

Yuan, T.-T., Kewley, L. J., & Sanders, D. B. 2010, ApJ, 709, 884